AIAA JOURNAL
Vol. 42, No. 9, September 2004

Unsteady Side Loads in a Thrust-Optimized Contour Nozzle at Hysteresis Regime

Sébastien Deck*
ONERA, 92322 Châtillon Cedex, France
and
Anh Thi Nguyen†
Ecole Nationale Superieure de Mecanique et d'Aérotechnique, 86036 Poitiers, France

Dangerous asymmetrical thrust components which act on the nozzle wall as side loads can occur during the low-altitude operating phase of a launcher when the flow is separated within the extension. To try to get a better understanding of this phenomenon, a numerical study of the unsteady side-loads occurring in a thrust-optimized contour nozzle is presented. Depending on the pressure ratio either a free shock or a restricted shock separation is observed with a significant hysteresis between these two flow regimes. The present effort is focused on a pressure ratio for which both shock patterns are observed at stationary conditions (hysteresis regime). The main features of the flowfield as well as the resulting side loads are described for both shock configurations. Statistical and spectral properties of side loads are analyzed and compared with the available experimental data. Finally, a semi-empirical method based on random pressure pulsations is suggested to assess the spectral distribution of side loads occurring in the free shock separation regime.

Nomenclature

$F(t)$	=	side-load norm, $\sqrt{[F_y^2(t) + F_z^2(t)]}$, N
$F_{y,z}(t)$	=	side-load component on y, z
M	=	Mach number
P	=	pressure, Pa
T	=	temperature, K
x, y, z	=	physical Cartesian coordinate axes, m
$\theta(t)$	=	angle between the side force and Ox axis, rad

Subscripts

a	=	ambient
c	=	chamber
w	=	wall
t	=	throat (geometry)

Introduction

THE first studies of nozzle separation were performed in overexpanded conical nozzles during the 1950s, leading to the Summerfield criterion.[1] The authors observed flow separation within the extension as soon as the wall pressure at the nozzle exit was lower than 0.4 times the ambient pressure. These studies were followed by the work of Lawrence,[2] who suggested a separation criterion using the plateau pressure rather than the ambient pressure P_a. In the early 1970s, Schmucker[3] provided the first semi-empirical method, based on the assumption of a tilted separation line, to estimate the side-load level. The measurements of Nave and Coffey[4] on the J2-S engine demonstrate clearly the existence of two flow regimes named, respectively, the free shock separation (FSS) and the restricted shock separation (RSS). In the first flow topology, the boundary layer separates from the nozzle wall and never reattaches on the wall, whereas the second shock pattern is characterized by a recirculation bubble with reattachment on the nozzle wall. During the transient startup, the separated flow is first governed by the FSS structure. This structure is then replaced by the RSS pattern when the chamber pressure exceeds a certain critical value. Hysteresis of FSS–RSS transition was also clearly identified. In 1996, a semi-empirical method for the prediction of the rms level of side loads caused by turbulent pressure pulsations was proposed by Dumnov.[5] Otherwise, the work of Pekkari[6] was based on an analysis of aeroelastic instabilities. In 1998, Frey and Hagemann[7] put emphasis on the distinction between FSS and RSS flows and on the RSS flow structure recovered by numerical simulations. More recently, the existence of reverse flow (trapped vortex) in the plume of thrust-optimized contour nozzles was demonstrated experimentally.[8] It is believed that the trapped vortex is linked with the caplike shock pattern, which can be interpreted as an inverse Mach reflection[9] of the internal shock at the nozzle axis.[10]

The side loads observed in an unadapted rocket nozzle are generally unsteady. The amplitude and direction of the nozzle change randomly with time. Engine designers are thus required to know not only the level of side-load magnitude but also its spectral distribution, which is very important for the dynamic response of the engine. Most of the previously mentioned side-load measurements were obtained with transient flow conditions.[11–15] The drawback of such an approach is that it precludes a classical analysis of the unsteadiness considered as fluctuations superimposed on a steady mean flow. To the authors' knowledge, the work of Nave and Coffey[4] on the J-2S engine is the only one that involved the measurement of side loads in the steady-state chamber conditions on a real engine. However, no information relating the spectral distribution and its evolution with chamber-to-ambient pressure ratio p_c/p_a were reported. The difficulty of recovering actual aerodynamic side loads from the dynamic response of the whole engine mechanical system has always been the main obstacle to overcome[16–18]

Because experimental side-load measurements are difficult to implement, numerical approaches appear very promising for the treatment of nonadapted flowfields in rocket nozzles. After the pioneering work of Chen et al., [19] whose calculations revealed a trapped vortex behind the central normal shock, there has been considerable interest in numerical approaches. Numerical investigations of shock patterns in rocket nozzles remained essentially a process of solving the averaged Navier–Stokes equations on steady axisymmetrical configurations.[20,21] Onofri et al.[22] and Nasuti and Onofri[23] got

Received 14 May 2003; revision received 14 January 2004; accepted for publication 18 March 2004.

*Research Scientist, 29 Av de la Division Leclerc.
†Ph.D. Student, Laboratoire d'Etudes Aérodynamiques, Centre National de la Recherche Scientifique, UMR 6609, 43 Route de l'Aérodrome.

interested in viscous and inviscid shock-generated vortices and pressure fluctuations in propulsive nozzles. More recently, Takahashi et al.[24,25] reported calculations on transient flow characteristics of rocket engine nozzles and Yonezawa et al.[26] studied startup and shutdown processes. The separation modes transition in the J2-S subscale rocket engine nozzle has been revisited by Morinigo and Salva.[27]

Nevertheless, not so many publications are devoted to numerical simulations of side loads because turbulent unsteady three-dimensional computations of a sufficient physical duration are required to reproduce the low-frequency characteristics of the separated mean flow in overexpanded nozzle flows. In 2002, studies[28,29] were presented of numerical simulations of side loads in an ideal truncated nozzle exhibiting pure FSS. The RSS was also investigated thanks to detached-eddy simulation[30] and calculations of side loads in the RSS regime can be found in the literature.[31] Yonezawa et al.[32] calculated the characteristics of flow pattern and shock structures for three different nozzles. These are, to the authors' knowledge, the only publications that present unsteady calculations of three-dimensional side loads in overexpanded rocket nozzles.

The current study involves the hysteresis regime observed in a thrust-optimized contour (TOC) nozzle designed by the German Aerospace Center and tested at Laboratoire d'Etudes Aérodynamiques (LEA) of Poitiers, France. The objective is twofold: 1) to assess the capability to capture numerically the hysteresis phenomenon widely observed in TOC nozzles and 2) to compare the side-load characteristics (including their statistical properties and spectral distributions) of two separation regimes (FSS and RSS) for the same pressure ratio, p_c/p_a.

Experimental Setup

An experimental study has been carried out on a subscale nozzle using a specific test facility. A schematic of the test setup used for this study is shown in Fig. 1. The nozzle is supplied with high-pressure dessicated air having a dew point of -70°C. The exit section of the nozzle is located in the external plane of the wall of the hall where the test facility is built. The ground is located at more than 20 nozzle exit diameters of the nozzle axis and the nearest obstacle is located at more than 80 diameters downstream of the nozzle lip. This geometric configuration is chosen to facilitate the comparison of experimental results with numerical simulations thanks to well-defined and simple boundary conditions. To avoid any aeroelastic effect, the nozzle was built to be very rigid with a first eigenmode at a frequency higher than 2 kHz.

Wall Pressure Measurements

Wall pressure measurements were performed with absolute Kulite transducers (model XCQ-062-25A) flush mounted on the nozzle wall. These transducers have a pressure-sensitive diaphragm of 0.71 mm in diameter and a range of 3.5×10^5 (Pa). A perforated screen protecting the diaphragm from dust particles limits the useful frequency bandwidth to about 50 kHz. The outputs from these transducers were directly amplified and then filtered by antialiasing programmable low-pass elliptic filters with a sharp roll-off. The signals were then digitized at 30 kHz per channel. The typical duration of a test is about 10 s, during which the variation of the stagnation pressure and temperature was less than 1%. The instantaneous wall pressures are then averaged to obtain the mean-timed wall pressure profiles used for comparison with unsteady three-dimensional computational results.

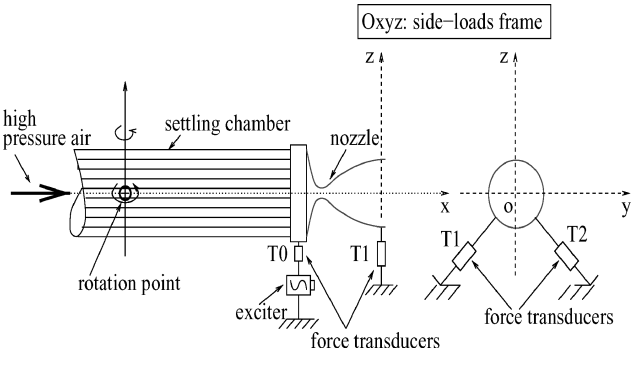

Fig. 1 Principle of the LEA test facility.

Side-Load Measurement

The side load is directly measured thanks to two force transducers, T1 and T2, mounted 10 mm upstream of the exit section of the nozzle. The angle between these transducers is 90 deg to determine the two components of the side-load vector. In fact, the loads measured by two force transducers during the test are the dynamic response of the mechanical system to aerodynamic excitation loads. To determine the true aerodynamic loads, the system frequency-response function must be determined. Let $\boldsymbol{F}_m(t)$ be the response of the system to the true aerodynamic excitation $\boldsymbol{F}_a(t)$, the Fourier transform of $\boldsymbol{F}_m(t)$, noted $\hat{F}_m(f)$, is related to that of $\boldsymbol{F}_a(t)$, noted $\hat{F}_a(f)$, by

$$\hat{\boldsymbol{F}}_m(f) = H(f)\hat{\boldsymbol{F}}_a(f) \tag{1}$$

where the transfer function $H(f)$ is determined by exciting the system by a known sinusoidal load measured by another transducer force T0 (Fig. 1). The true aerodynamic excitation $\boldsymbol{F}_a(t)$ is finally obtained by taking the inverse Fourier transform (named here for convenience $\mathcal{F}^{-1}$) of relation (1):

$$\boldsymbol{F}_a(t) = \mathcal{F}^{-1}\left[H^{-1}(f)\hat{\boldsymbol{F}}_m(f)\right] \tag{2}$$

Numerical Approach

Numerical Method

The equations solved here are the unsteady, three-dimensional Reynolds-averaged compressible Navier–Stokes (URANS) equations with a turbulence model used for closure. The perfect gas relation and a constant ratio of specific heats are used in the computation. The FLU3M code, which is used to calculate the separated nozzle flow, was validated from low-subsonic to hypersonic flows. It solves the Navier–Stokes equations on multiblock structured grids. The computational domain is divided by blocks; each block is composed of structured hexahedral cells. The Navier–Stokes equations are discretized using a second-order space upwind finite volume scheme and a cell-centered discretization. Roe's flux difference splitting scheme is employed to obtain advective fluxes at the cell interface. The MUSCL approach extends the spatial accuracy to second order and is combined with minmod or Van Albada's limiters. All viscous terms are centrally differenced.

Unsteady (global time-step) and three-dimensional Navier–Stokes simulations are highly CPU demanding. Indeed, explicit schemes are not efficient enough for this purpose and implicit schemes are required. Time discretization is based on second-order accurate Gear's formulation and was introduced by Péchier[33] during his thesis. Moreover, the implicit formulation results in the inversion of a large sparse matrix system. The lower–upper (LU) factorization simplifies the inversion of the latter implicit system. Further details concerning the numerical method can be found in the literature.[34] Because of the experimental low-frequency characteristics of the fluctuating side load (frequency range of interest 0–200 Hz),[35] the attempt to use a URANS approach is legitimate. Indeed, the mean flow frequency characteristics are much lower than characteristic frequencies of the turbulent motion. The turbulence model used here is an algebraic model based on Goldberg's backflow formulation.[36,37] Further details concerning the overall model can be found in the literature.[28]

Grids

To evaluate the accuracy of the different simulations, two grids have been built. The three-dimensional grid has been obtained by rotating a two-dimensional grid around the nozzle axis (Fig. 2). Each grid is divided into two blocks. The first block is used to mesh the nozzle, and the second one concerns the external region after the exhaust. The i direction corresponds to the axial direction. The j direction is the radial one normal to the axis and k represents the

different planes around the nozzle axis. The density of the different grids is summarized in Table 1.

Figure 3 presents the value y^+ at the first mesh point above the solid surface of grid A (reference grid) for both shock patterns at the same pressure ratio. One can notice that y^+ always stays below 0.5 for FSS and below 2 downstream of the reattachment of the supersonic jet occuring in the RSS regime, which is quite sufficient for a correct calculation of the viscous stresses. It has been verified[38] thanks to steady axisymmetrical RANS calculations that with this resolution grid convergence is achieved for the mean field. This fine grid has then been retained as a reference grid in the symmetry plane. One issue of this work is to evaluate the grid convergence for a three-dimensional unsteady calculation from a statistical point of view. Hence, grid B allows evaluation of the influence of the number of radial planes (one every 5 deg instead of 7.5 deg in reference grid A), that is, the effect of the grid refinement in the azimuthal direction.

Computation Description

This numerical study is focused on a pressure ratio of 17.5 where two types of flow separation are observed (both experimentally and numerically) depending on the flow history. FSS was obtained numerically by increasing the pressure ratio from 15 to 17.5 while RSS was obtained by decreasing the pressure ratio from 20 to 17.5.

To ensure the time accuracy of the results, the physical time step, Δt_{CFD}, of the simulation is taken equal to 5μs, which is compatible with an accurate simulation of 200-Hz phenomena. Due to experimental low frequencies[35,38] of the fluctuating side loads, the simulation has to be performed on a total duration long enough to get the correct statistical properties of these phenomena. On the other hand, the length of the signal is limited by the high CPU cost of unsteady three-dimensional turbulent flow calculations. This aspect will be discussed more precisely in the following.

The main characteristics of the computation are summarized in Table 1. The useful unsteady computation was performed over $N = 300{,}000$ time steps with a total duration of $T = 1.5$ s. The number of samples used for the statistical analysis is equal to 30,000. The computational cost was about 235 CPU hours for the finest grid (2.75 million grid points) on an NEC SX5 supercomputer. Hence, the CPU cost per cell and per iteration was equal to 1.2 μs.

Table 1 Computation characteristics

Parameter	Grid A	Grid B
Nozzle ($i \times j \times k$)	$161 \times 100 \times 49$	$161 \times 100 \times 73$
Exterior ($i \times j \times k$)	$120 \times 180 \times 49$	$120 \times 180 \times 73$
No. of nodes N_{xyz}	1,850,000	2,752,000
Time step Δt_{CFD}	5 μs	5 μs
Frequency sampling $f_e = 1/T_e$	20 kHz	20 kHz
No. of iterations N	300,000	300,000
No. of samples M	30,000	30,000
Time of integration $T = N\Delta t_{\mathrm{CFD}} = MT_e$ (s)	1.5 s	1.5 s
CPU cost on an NEC SX5	≈160 h	≈235 h

Results and Discussion

Flowfield Description

The flow at full-flowing condition (see Fig. 4) is characterized by the occurrence of an internal shock emanating from a region fairly close to the throat, that is, where the circular arc forming the nozzle throat turns into the further expansion contour. This shock is slightly bent and converges toward the nozzle axis farther downstream. This internal shock divides the core flow in two parts, a high-speed, high-momentum flow region near the symmetry axis and a high-pressure level region near the wall. Further details on this internal shock generation in thrust-optimized rocket nozzles are given in Ref. 7.

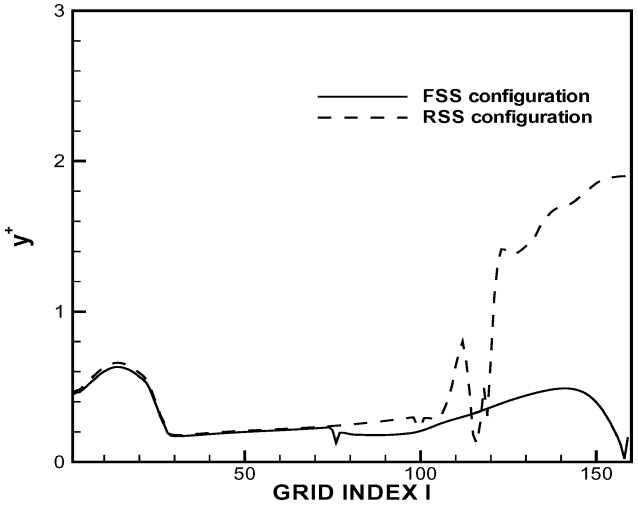

Fig. 3 Value y^+ size of neighboring cells.

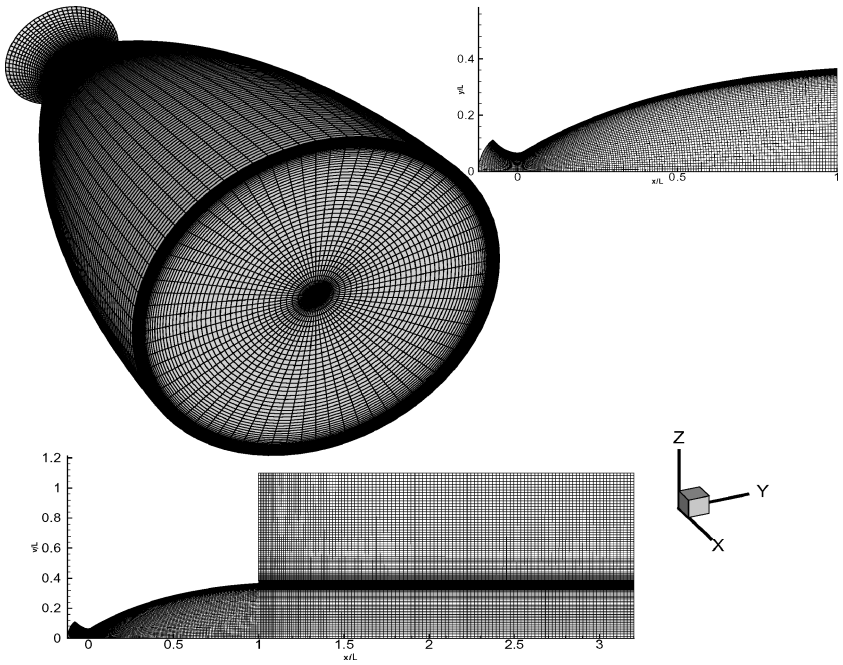

Fig. 2 Three-dimensional grid of the LEA TOC nozzle.

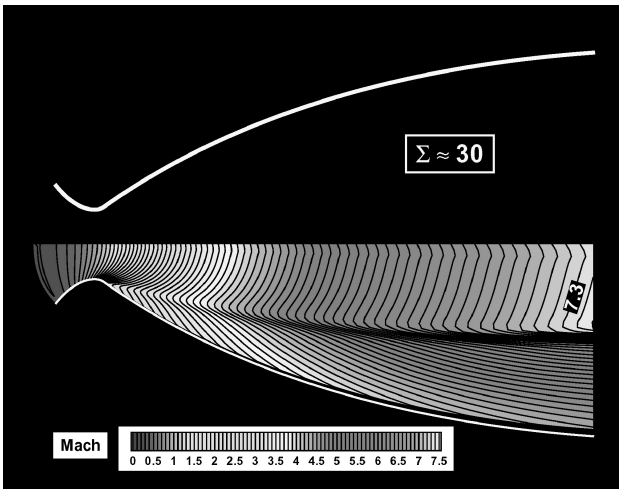

Fig. 4 Iso-Mach contours in full-flowing regime.

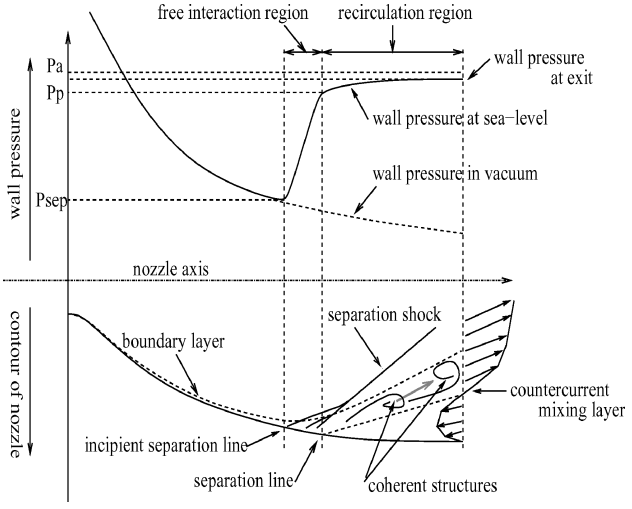

a) FSS regime

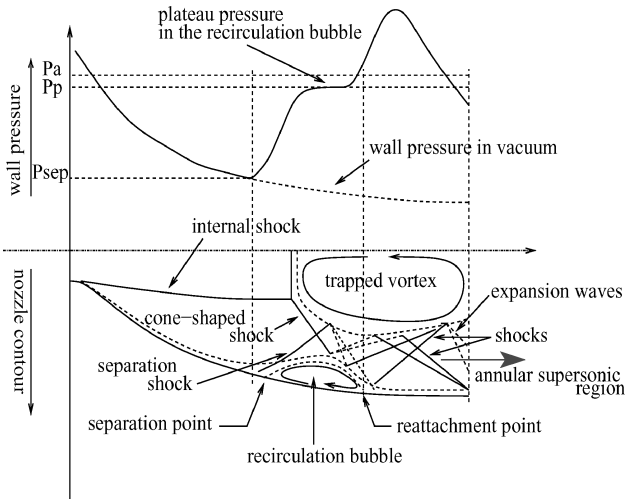

b) RSS regime

Fig. 5 Sketch of the flow in overexpanded regime.

In the overexpanded regime (e.g., when the chamber pressure is not high enough to reach full flow in the extension), a shock forms to adjust the jet static pressure to the ambient pressure. In a TOC nozzle, two shock patterns could be observed according to the pressure ratio.[39] During the transient startup phase, for the lowest pressure ratio, the separated flow is first governed by the FSS structure, whose description is presented in Fig. 5a, along with the wall pressure distribution. Separation and subsequent formation

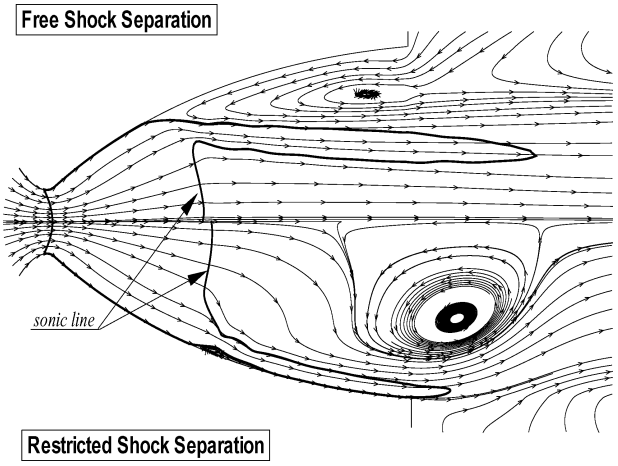

Fig. 6 Averaged sonic line and streamlines in hysteresis regime (pressure ratio, 17.5).

of a recirculation zone induce an oblique shock wave near the wall. This oblique shock results in an abrupt rise of the wall pressure. Downward of the separation, the wall pressure reaches a plateau. Downstream of this plateau, the wall pressure increases slowly up to a level slightly lower than the ambient pressure. This shock pattern is called FSS because, once separated, the flow does not reattach and continues as a free jet.

The presence of an internal shock and the inverse Mach reflection of the latter results in a peculiar shock pattern called caplike shock. The cone-shaped shock, which is a part of the caplike shock structure, tends to force the separated boundary layer to reattach on the nozzle wall. Depending on the balance between the radial momentum induced by the cone-shaped shock and the separation shock, one can have either the classical FSS structure or another structure called RSS as illustrated in Fig. 5b. Because of the reflections of the shocks and expansion waves in the annular supersonic region limited between the wall and the low-speed recirculating annular vortex (trapped vortex), the mean wall pressure is subjected to large variations which may reach values much higher than the ambient atmospheric pressure.

Figure 6 shows the time- and space-averaged (in the azimuthal direction) sonic line and streamlines issued from the unsteady three-dimensional simulation of two separation regimes obtained for $p_c/p_a = 17.5$. The upper part presents the FSS, which is reached while the chamber pressure is increased (i.e., $\partial PR/\partial t > 0$). This figure highlights the external ambient flow, which is sucked into the nozzle and finally evacuated by the entrainment effect of the jet.

The lower part presents the RSS, which occurs if $\partial PR/\partial t < 0$. The RSS structure at $p_c/p_a = 17.5$ was obtained experimentally by first increasing the chamber pressure to a value higher than the value at which the transition FSS $\rightarrow$ RSS occurs during the transient startup phase. The chamber pressure was then slowly decreased to obtain the RSS configuration at $p_c/p_a = 17.5$.

The corresponding computed averaged field is characterized by a stable vortex that is trapped downstream of the normal shock while there is no recirculation behind a Mach disk. Also worth noting is the longitudinal shift farther downstream of the separation compared to the corresponding FSS regime.

The mean-time wall pressures are shown in Fig. 7 and compared with experimental data. The computed mean separation point of the FSS configuration is found farther downstream of the experimental one. To test the grid convergence, the computations were performed for two different grids, A and B. The differences between the results yielded from the two grids are very small and grid convergence is almost achieved. If the reasoning of Frey and Hagemann[7] relating the cause of the reattachment of the separated flow is correct, this overestimation of the separation point will result in a premature transition of FSS to RSS compared to the experiment. Effectively, numerical computation using this code gives a stable RSS configuration for a pressure ratio lower than 24, which experimentally

involves an FSS configuration during the increasing phase of chamber pressure (i.e., $\partial PR/\partial t > 0$). The computation seems to give a better prediction of the separation point in the RSS regime. This may be due to the fact that the flow in the vicinity of the separation point in the RSS configuration is subjected to a lower pressure gradient; the behavior of the turbulence model is thus much better. The plateau pressure p_p measured in the recirculation bubble formed between the separation and reattachment lines is much lower than ambient pressure. This explains why the separation line is located farther downstream in the RSS regime.

Asymmetrical Flow Separation

Once the separation occurs, the flow loses its axisymmetrical nature as illustrated in Fig. 8, which shows the instantaneous skin friction lines for both separated configurations. The separation and reattachment lines are evidenced numerically by an accumulation of skin friction lines. It is worthwhile to notice the asymmetry of the instantaneous reattachment line occurring in the RSS regime as well as the lip-reattachment line for the FSS. This result supports Nave and Coffey's[4] assumption that the side loads observed in the RSS regime are due essentially to an asymmetric reattachment of the separated flow.

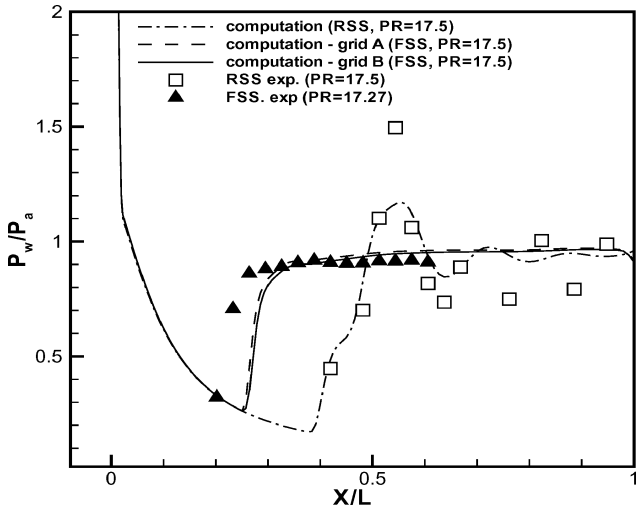

Fig. 7 Averaged wall pressure distribution in hysteresis regime (pressure ratio, 17.5).

Afterward, the mean steady wall pressure data obtained by experiments were plotted together with the instantaneous wall pressure obtained numerically for both separation regimes (see Fig. 9). The different curves correspond to different meridian lines. The discrepancies among these curves demonstrate the asymmetric nature of the separated flow. It is worth noting that in both cases the wall pressure distribution is perfectly axisymmetric upstream of the separation line because a steady incoming boundary condition is used. One observes, however, the three-dimensional nature of the flowfield downstream of the separation line.

In the FSS regime, the dissymmetry is much more pronounced at the middle of the recirculation region and at the nozzle exit. Important discrepancies of the wall pressure observed at the nozzle exit are obviously due to the asymmetric reattachment line of the secondary recirculation bubble formed at the nozzle exit, as shown in Fig. 8. The countercurrent mixing layer formed between the ambient atmospheric air sucked into the nozzle and the main separated supersonic jet can support absolute instability[40] which, once established, affects the entire flow. The absolute instability, if any, may be the origin of unsteadinesses of the separated flow occurring in the FSS regime. Further experiments are under study at LEA to elucidate this point.

In the RSS regime, the dissymetry of wall pressure is much more pronounced downstream of the reattachment line where the meantime wall pressure displays an important gradient. The origin of the unsteadiness observed in the RSS regime is not clear. It seems that the perturbations coming from downstream and propagating through the subsonic region found downstream of the caplike shock structure is the cause of these unsteadiness. These results again confirm the assumption of Nave and Coffey[4] that the side loads observed in the RSS regime are essentially due to an asymmetric reattachment of the separated flow.

Statistical Analysis

Side-Load Components

Figure 10 shows a typical polar plot, $F_z(t)$ vs $F_y(t)$, of experimental side loads for the FSS regime. Similar behavior is observed for the RSS. One can notice the isotropic and random character of the fluctuating side loads.

To evaluate whether the computational time is long enough to get correct statistical properties of side loads, a first criterion is to qualify the statistical isotropy of the computed side load because, for an axisymmetrical geometry, no particular direction has to be privileged. To this end, let us consider the bidimensional random variable $\tilde{F} = (F_y, \quad F_z)^t$ defined by its mean value $M = [\overline{F_y} \quad \overline{F_z}]^t$ and its

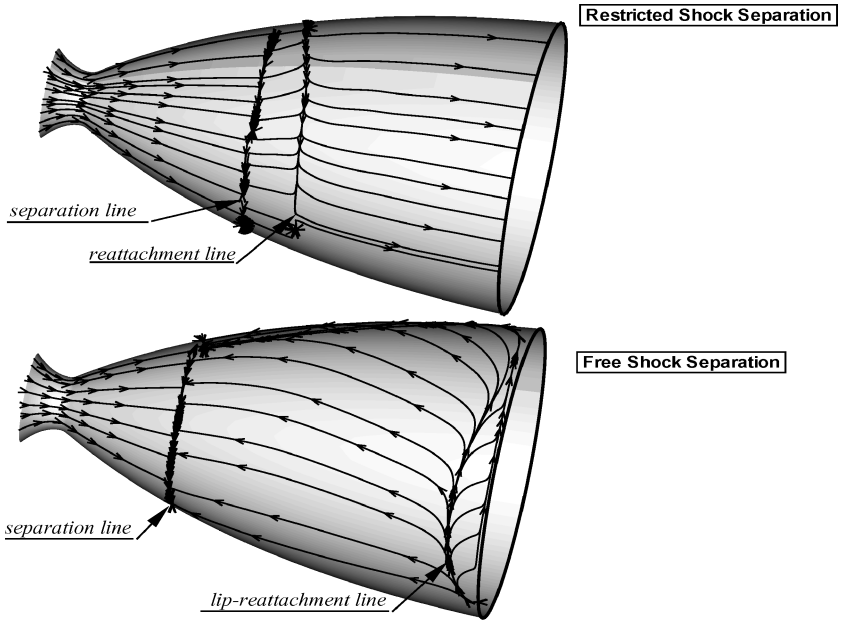

Fig. 8 Instantaneous skin friction lines in hysteresis regime (pressure ratio, 17.5).

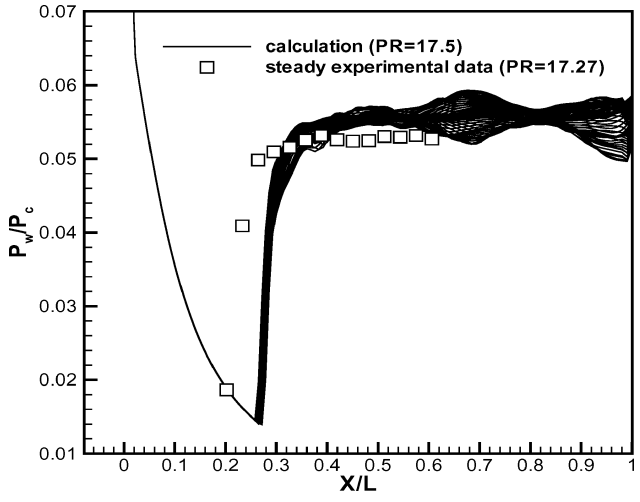

a) FSS regime

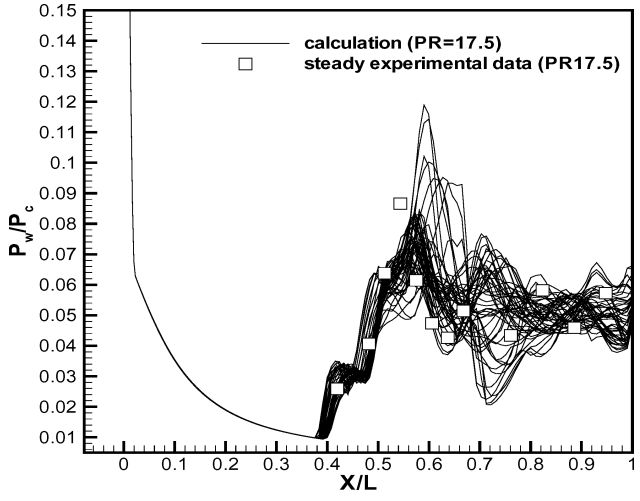

b) RSS regime

Fig. 9 Instantaneous wall pressure distribution.

covariance matrix $C = \overline{\tilde{F}\tilde{F}^t} - MM^t$. We suppose that the determinant of the covariance matrix is not equal to zero. The joint probability density function (PDF) enables one to establish a probabilistic description for the side load that is associated with the two F_y and F_z components. The joint distribution of $\tilde{F}$ is said to follow a two-dimensional Gaussian distribution if its PDF is given by

$$p_{\tilde{F}}(F_y, F_z) = \left(1/2\pi\sqrt{\det C}\right) \exp\left[-\tfrac{1}{2}(\tilde{F} - M)^t C^{-1}(\tilde{F} - M)\right] \quad (3)$$

To characterize the couple (F_y, F_z), let us consider a set of points of the plan defined by

$$\Delta(\xi) = \left\{\tilde{\boldsymbol{F}} = (F_y, F_z) \in \boldsymbol{R}^2 \Big/ (\tilde{\boldsymbol{F}} - \boldsymbol{M})^t C^{-1}(\tilde{\boldsymbol{F}} - \boldsymbol{M}) < \xi\right\} \quad (4)$$

whose boundary in $\boldsymbol{R}^2$ space is defined by the ellipse of

$$(\tilde{\boldsymbol{F}} - \boldsymbol{M})^t C^{-1}(\tilde{\boldsymbol{F}} - \boldsymbol{M}) = \xi \quad (5)$$

The joint Gaussian probability density function is easily described in terms of equiprobability ellipses. It can be shown that the percentage of observation in the whole plane outside this ellipse defined by ξ is αN, where N is the size of the sample and α, which can be interpreted as a level of confidence, is defined by

$$\alpha = \int_{\Delta(\xi)} p_F(F_y, F_z)\, \mathrm{d}F_y\, \mathrm{d}F_z \quad (6)$$

Moreover, it can be shown that α and ξ are linked by the relation

$$\xi = 2\log(1 - \alpha) \quad (7)$$

To apply this result, one might calculate Eq. (7) for 0.05% values. This gives the ellipse, which includes 95% of the observations (see Figs. 11 and 12) for FSS and RSS regimes, respectively). The number of points outside the equiprobability ellipse, $N_{\text{computation}}$, can then be compared with the theoretical number, $N(1 - \alpha)$, corresponding to two-dimensional Gaussian distribution.

Moreover, if the covariance matrix is symmetric (i.e., $\sigma_{F_y} = \sigma_{F_z}$), the ellipse becomes a circle. This circle has to be centered at zero because, for an averaged axisymmetrical flow, the side loads are absent; that is, $\overline{F_y} = \overline{F_z} = 0$. Hence, the side-load components F_y and F_z can be considered two independent random variables with

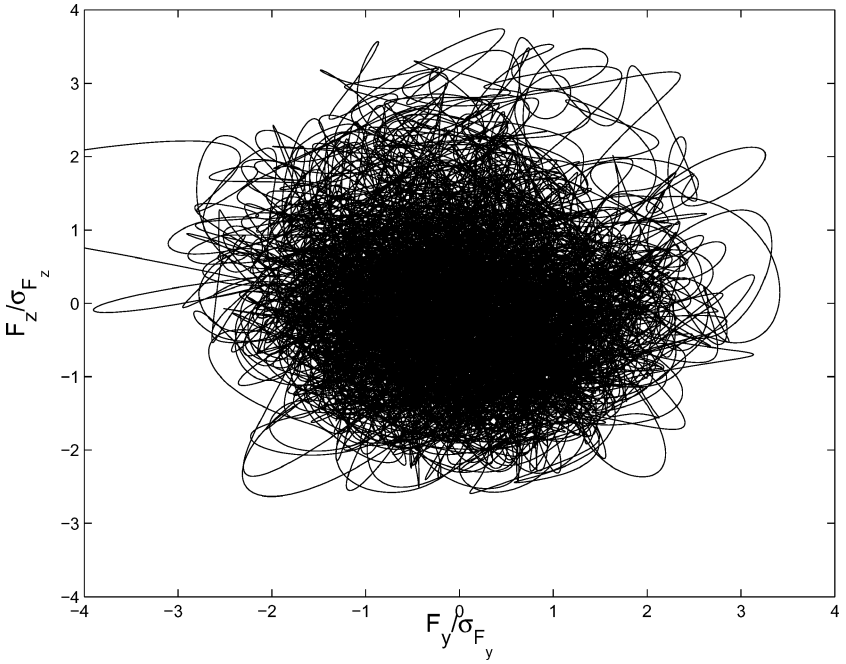

Fig. 10 Typical experimental polar plot (FSS; pressure ratio, 17.27).

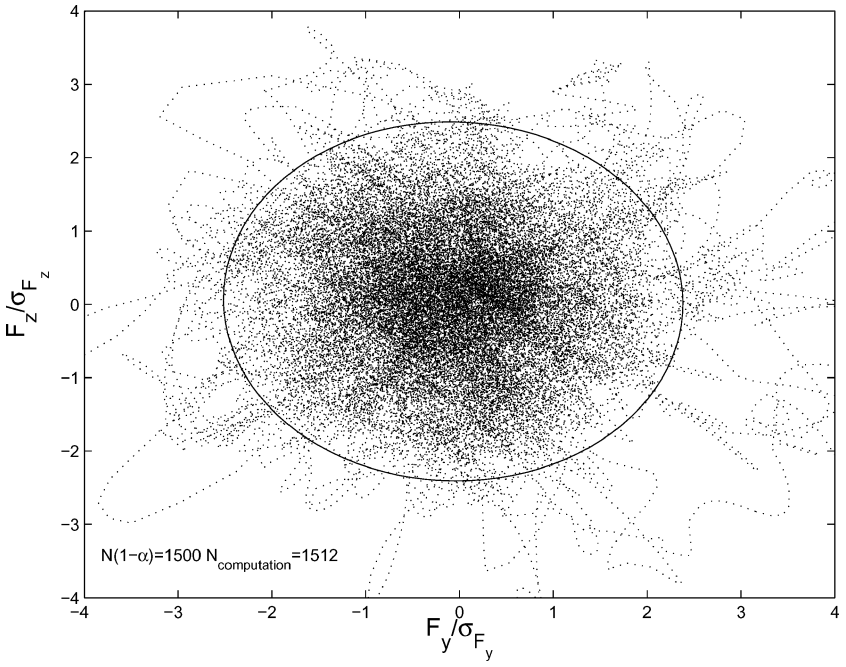

Fig. 11 Computed polar plot and 95% confidence ellipse (FSS; pressure ratio, 17.5).

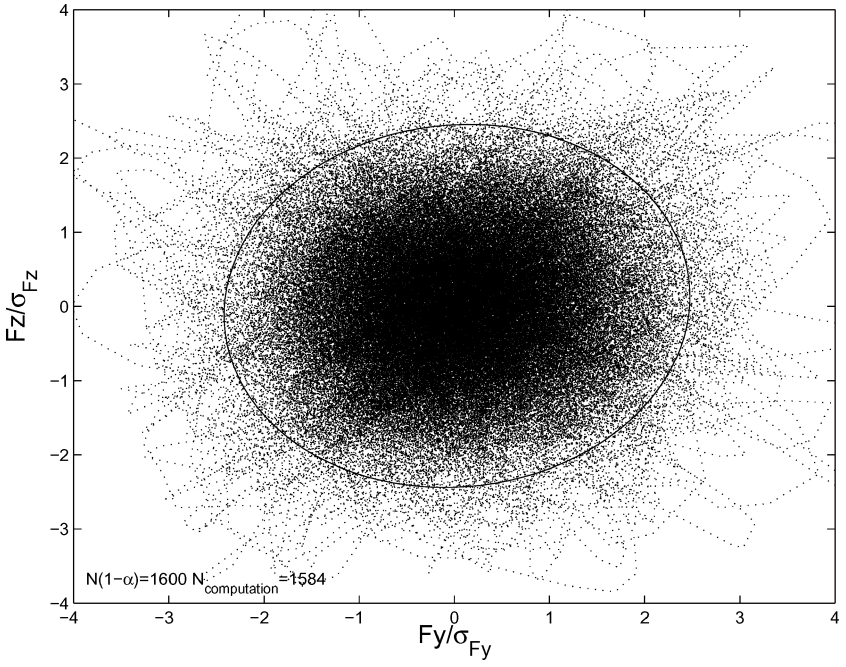

Fig. 12 Computed polar plot and 95% confidence ellipse (RSS; pressure ratio, 17.5).

zero mean and the same variance. This allows us to qualify, from a statistical point of view, the isotropy of the computed side load.

Side-Load Magnitude and Direction

To complete and define properties of magnitude and direction of the side loads caused by random pressure fluctuations, a statistical description is needed. There are numerous ways to define probability, but from an engineering point of view the most convenient definition is in terms of relative frequency of occurrence. Indeed, it is interesting to take into account the PDF of the side-load magnitude and direction. The computed side-force probability density function is compared with experimental results obtained by LEA in Fig. 13. First, it is worthwhile to note that both shock patterns lead to identical statistical properties of the side-load magnitude. Both values indicate that the distribution of side-load amplitude is a Rayleigh distribution (as suggested by Dumnov[5] and several other authors[28,41]) whose PDF is described with the following relation:

$$p(F|\lambda) = F\Big/\lambda^2 e^{-F^2/2\lambda^2}, \qquad x \geq 0$$
$$0, \qquad \text{otherwise} \tag{8}$$

where F is the random value of the side-load amplitude, λ is a parameter such that

$$\lambda = \sqrt{\frac{1}{2N}\sum_{i=1}^{N} F_i^2}$$

(most likelihood estimator), and N is the size of the sample.

Herein, it is worth comparing the mean side-load magnitude and standard deviation with the theoretical values of a Rayleigh distribution given, respectively, by

$$\bar{F} = \lambda\sqrt{\pi/2}, \qquad \sigma_F^2 = [(4-\pi)/2]\lambda^2 \tag{9}$$

Table 2 Comparison between calculation and Rayleigh's distribution

RP	$\bar{F}/F_{\text{rms}}$	Rayleigh value	Δ, %	σ/F_{rms}	Rayleigh value	Δ, %
FSS, calc.	0.906	0.886	2.3	0.420	0.463	9.2
RSS, calc.	0.873	0.886	1.4	0.496	0.463	7.1

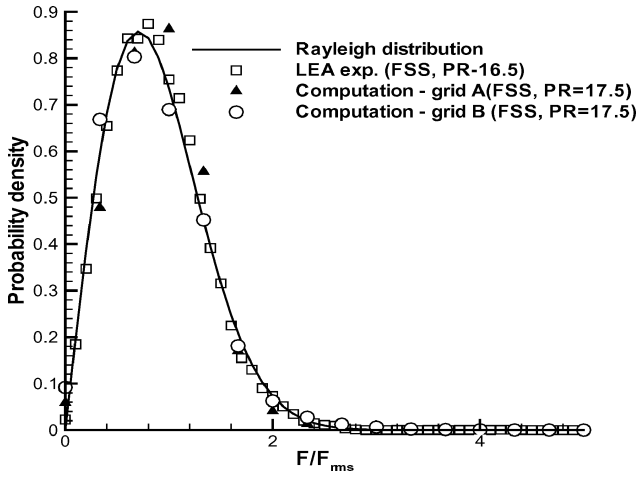

a) FSS regime

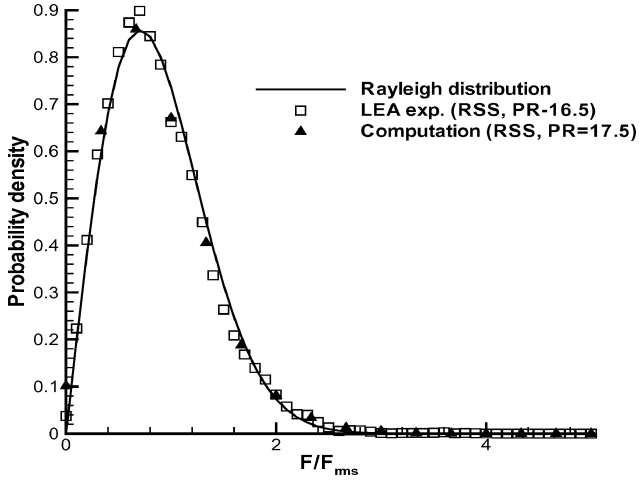

b) RSS regime

Fig. 13 PDF of side-load amplitude.

Comparison results are summarized in Table 2. One can notice that computed values differ by less than 10% from those given by Eq. (9). These results could be quite expected for an axisymmetrical geometry because the Rayleigh distribution is the particular case of a χ^2 distribution with two degrees of freedom, which correlates with normally distributed side-load components.

Figure 14 compares the computed PDF of the side-load direction for both shock patterns with experimental results. One can notice that for both shock patterns the experimental and computed PDFs of the side-load direction fluctuate around the uniform law within the interval $[0; 2\pi]$ (or [0; 360] deg) defined by

$$p(\theta) = 1/2\pi, \qquad 0 < x \leq 2\pi$$
$$0, \qquad \text{otherwise} \tag{10}$$

This can be proven by calculating higher-order moments of phase fluctuations which can then be compared with theoretical values of the uniform distribution. The results of these comparisons are shown in Tables 3 and 4 for experiment and calculation, respectively.

Experimental data are in very good agreement with theoretical statistical moments issued from a uniform distribution. The skewness factor S_θ equal to zero illustrates the symmetry of the distribution, that is, no direction is privileged. Moreover, the value of

Table 3 Comparison of statistical moments between experiment and the uniform distribution

Statistical moment	Uniform law	FSS, exp.	Δ, %	RSS, exp.	Δ, %
$\bar{\theta}/\pi$	1	1.008	0.8	0.995	0.5
σ_θ^2/π^2	$\frac{1}{3}$	0.314	5.8	0.344	3.25
$S_\theta = \overline{\theta'^3}/\overline{\theta'^2}^{\frac{3}{2}}$	0	9.10^{-4}	0.1	8.10^{-3}	0.8
$K_\theta = \overline{\theta'^4}/\overline{\theta'^2}^2$	$\frac{9}{5}$	1.87	3.9	1.82	1.2

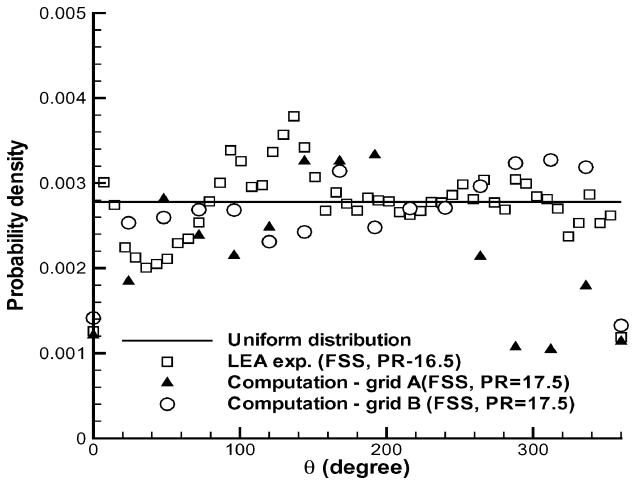

a) FSS regime

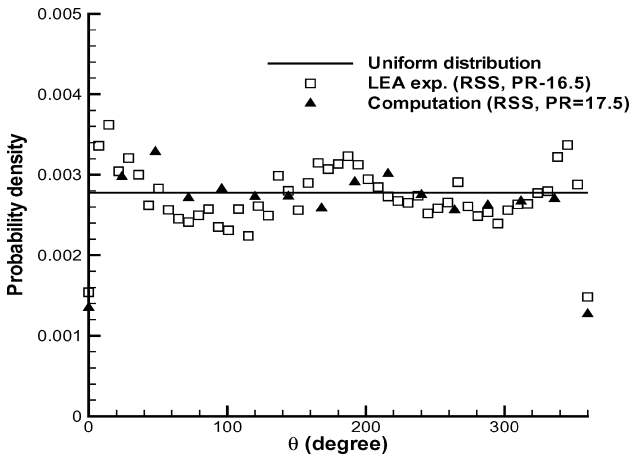

b) RSS regime

Fig. 14 PDF of side-load direction.

the kurtosis factor K_θ equal to 1.8 highlights that the direction does not follow a Gaussian distribution ($K_\theta = 3$). Computed moments mostly compare favorably except for higher moments, in particular in the FSS regime. These discrepancies can be attributed to the total duration of the unsteady calculation ($T = 1.5$ s), which is probably not enough to converge fourth-order statistical moments.

Finally, the experiments as well as the calculations suggest that, for both shock patterns, the side loads can be seen as a rotating vector uniformly distributed within the interval $[0; 2\pi]$ and whose magnitude follows Rayleigh's law.

Spectral Analysis

The power spectral density (PSD) function $G(f)$ describes how the root mean squared value of side loads is distributed in the frequency domain.[42] PSD functions are computed using the Welch[43] method. This method consists of dividing the effort components time data into overlapping segments with 50% overlap, computing a modified periodogram of each segment, and then averaging the PSD estimate. Moreover, because of numerical short data records (due to high CPU cost), it is very important in interpreting spectral estimates to be able to determine whether a particular spectral detail

Table 4 Comparison of statistical moments between calculation and the uniform distribution

Statistical moment	Uniform law	FSS (grid A)	Δ, %	FSS (grid B)	Δ, %	RSS	Δ, %
$\overline{\theta}/\pi$	1	0.988	1.2	1.038	3.8	0.979	2
σ_θ^2/π^2	$\frac{1}{3}$	0.253	42	0.339	1.8	0.33	<1%
$S_\theta = \overline{\theta'^3}/\overline{\theta'^2}^{\frac{3}{2}}$	0	0.1	10	−0.1	10	0.04	4
$K_\theta = \overline{\theta'^4}/\overline{\theta'^2}^2$	$\frac{9}{5}$	2.26	25	1.77	16	1.79	0.5

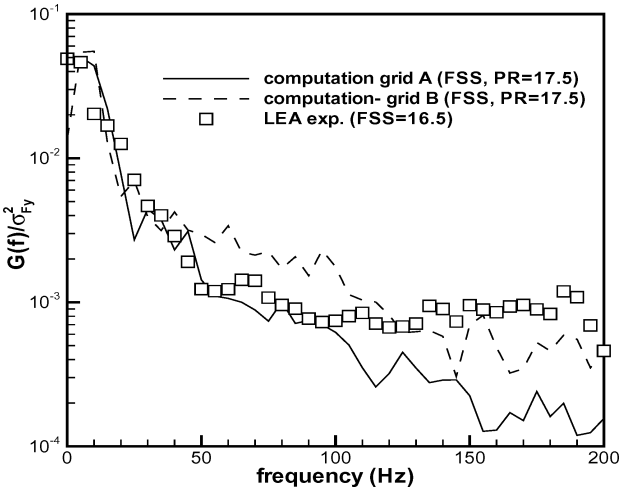

Fig. 15 PSD of the F_y component of side load in FSS regime in the frequency range 0–200 Hz.

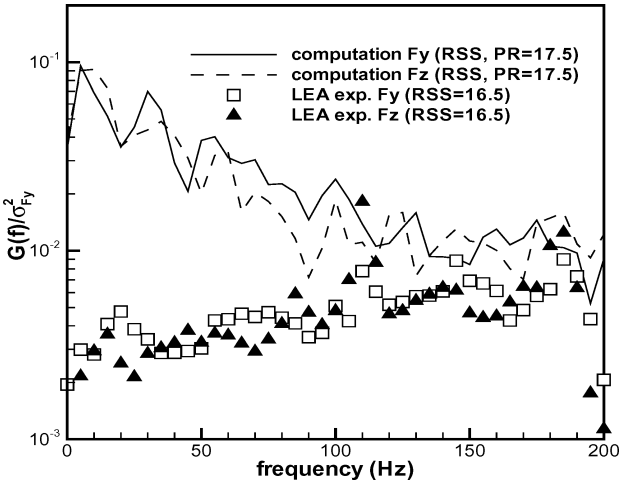

Fig. 16 PSD of the side-load components in RSS regime in the frequency range 0–200 Hz.

is due to statistical fluctuation or is actually present. Hence, we need some measures of confidence in the spectral estimate. Kay[44] gives a $(1-\alpha)\times 100\%$ confidence interval of this PSD estimate where α is the level of significance.[42]

Figure 15 compares the one-sided PSD function $G(f)$ for the FSS regime between calculations and experiments. These spectra issued from the simulations have been obtained by using 14 overlapping segments with a Hanning tapering window leading to a frequency resolution of 5 Hz. Assuming these parameters, a 95% confidence interval may be given by $[0.6G(f); 2, 5G(f)]$. This interval appears rather large and illustrates the main difficulty in simulating low-frequency phenomena. Spectra for both grids are also presented. It is worthwhile to note that in the FSS regime the side loads are dominated by very low frequencies. This aspect has also been observed for a truncated ideal contour nozzle exhibiting only FSS.[35,38]

The PSD obtained for the RSS regime is shown in Fig. 16. More discrepancies between calculations and experiments than for the free shock pattern are observed in the frequency range [0, 200 Hz]. These discrepencies may be due either to the uncertainty of the numerical

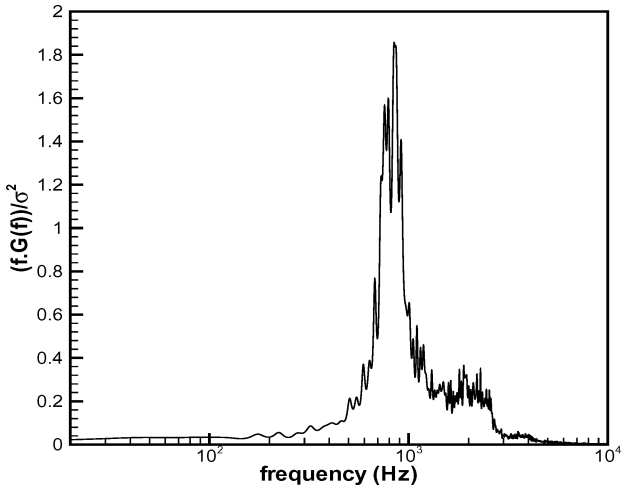

Fig. 17 PSD of the computed F_y component in the RSS regime.

simulation to correctly calculate very-low-frequency phenomena or to the experimental difficulty to correctly recover very low side-load levels in the frequency range [0, 200 Hz] for the RSS regime. Figure 17 presents the normalized PSD function $f * G(f)/\sigma^2$ of the y component of the side loads. This format results in a power spectral curve that has an area below it equal to unity. This fact more readily permits identification of dominant frequencies.[42] One can see that side loads occurring in the RSS regime exhibit much higher frequencies than in the FSS regime. It is worth noting that the frequency range 0–200 Hz only contributes to 30% of the total variance of the side-load component, that is,

$$\beta_{\mathrm{RSS}} = \frac{\sqrt{\int_0^{200} G_{\mathrm{RSS}}(f)df}}{\sigma} \approx 0.3$$

while $\beta_{\mathrm{FSS}} = 0.9$. The experimental setup does not allow verification of this hypothesis concerning the RSS due to the difficulty in correctly determining the transfer function for frequencies higher than 200 Hz. These results are very important because they show that side loads in FSS and RSS regimes have a very different frequency distribution. More precisely, the FSS regime is characterized by very low frequencies, whereas the RSS regime exhibits higher frequencies with a peak centered around 700 Hz.

Semi-Empirical Side-Load Estimation Model

Most of the existing empirical and semi-empirical side-load models permit estimation only of the magnitude of side loads. The semi-empirical model proposed by Dumnov[5] is, to the authors' knowledge, unique and the first model that offers the possibility of estimating the spectral distribution of side loads. The most important data required by Dumnov's model are the cross-spectral distributions of the nozzle's complete wall pressure field. These data are extracted from a subscale model and then generalized and applied to any nozzle. This model undergoes certain weaknesses and needs to be improved.

Explicitly, determining the aerodynamic side loads from the instantaneous pressure field allows one to get around the inertia correction problem. However, the instrumentation required for measuring the complete pressure field would be too expensive. In the following, an easier method is proposed enabling estimation of the PSD of side loads in the FSS regime. This method uses simply the pressure

data along two opposite generating lines rather than the complete pressure field.

In an axisymmetric nozzle, the PSD of side loads relates to that of the wall pressure fluctuations by the following relation suggested by Dumnov[5]:

$$S_{F_\phi}(f) = 2\pi \int_0^\pi \int_0^L \int_0^L S_{pp}(x_1, x_2, \Delta\phi, f) \times \cos\Delta\phi r(x_1)\, r(x_2)\, \mathrm{d}x_1\, \mathrm{d}x_2\, \mathrm{d}\Delta\phi \quad (11)$$

where $S_{pp}(x_1, x_2, \Delta\phi, f)$ denotes the cross-spectral density of random pressure fluctuations and f, x_i, and $\Delta\phi$ are frequency, longitudinal, and azimuthal coordinates, respectively.

The fluctuating pressure field, being a periodic function of the azimuthal angle ϕ, can be expanded in Fourier series:

$$p(x, \phi, t) = P_{a0}(x, t) + \sum_{k=1}^{\infty} [P_{ak}(x, t)\cos(k\phi) + P_{bk}(x, t)\sin(k\phi)] \quad (12)$$

Let $S_{P_{ak}P_{am}}$ be the cross-spectral density of the coefficients $P_{a_k}(x, t)$ and $P_{a_m}(x, t)$.

If the flow is statistically homogeneous in the azimuthal direction, then one can show that the cross-spectral density of the pressure fluctuations can be written as follows:

$$S_{pp}(x_1, x_2, \Delta\phi_1, f) = \sum_{k=0}^{\infty} \cos(k\Delta\phi) S_{P_{ak}P_{ak}}(x_1, x_2, f) \quad (13)$$

It is obvious from Eqs. 11 and 13 that, due to orthogonality properties of the trigonometrical function in the range $[0; 2\pi]$, only the first mode ($k = 1$) contributes to the side loads.

In the FSS regime, analyses of wall pressure fluctuations[45] show a relatively important coherence between two points oppositely located on the same meridian plane for frequencies less than 200 Hz. The phase features a difference of 180 deg. If one assumes that, for frequencies less than 200 Hz, the wall pressure fluctuation field is dominated by the first mode, the side loads in this frequency range may thus be evaluated by using simply the wall pressure data along two opposite generating lines ($\Delta\phi = 180$ deg). This hypothesis seems to be more legitimate for the averaged pressure $\bar{p}(\phi, t)$ obtained by integrating the wall pressure field $p(x, \phi, t)$ along x:

$$\bar{p}(\phi, t) = \frac{\int_0^L p(x, \phi, t)\, r(x)\, \mathrm{d}x}{L^2} \quad (14)$$

where L is the distance from the incipient separation point to the nozzle exit. The PSD of the y component of side loads may finally be determined by

$$S_{F_y}(f) = \mathcal{F}\left[\int_0^{2\pi} \int_0^L p(x, \phi, t) r(x) \cos\phi\, \mathrm{d}x\, \mathrm{d}\phi\right] = L^4\pi^2 S_{\bar{P}_{a_1}}(f) \quad (15)$$

where $\mathcal{F}$ denotes the Fourier transform and $S_{\bar{P}_{a_1}}(f)$ is the PSD of the coefficient $P_{a_1}(\mathrm{t})$ of the cosinus term of the first mode ($k = 1$) in the Fourier decomposition of $\bar{p}(\phi, t)$:

$$\bar{p}(\phi, t) = \bar{P}_{a_0} + \sum_{k=1}^{\infty} \left[\bar{P}_{a_k}(t)\cos(k\phi) + \bar{P}_{b_k}(t)\sin(k\phi)\right] \quad (16)$$

The coefficient $P_{a_1}(\mathrm{t})$ may then be estimated simply by using the wall pressure data along two opposite generatrice lines if one assumes the averaged pressure field $\bar{p}(\phi, t)$ is dominated by or, more precisely, involves only the first mode.

The PSD of the $F_y(t)$ component estimated by this method is shown in Fig. 18 and compared with computational and experimental results. One can observe a very good agreement between PSD estimated by this method and that yielded by integrating the complete field of wall pressure $p(x, \phi, t)$ (dashed line).

It is important to note that this model relies on the hypothesis that the averaged pressure field $\bar{p}(\phi, t)$ is dominated by the first mode (at least for the low frequencies, where two points oppositely located on the same meridian plan show an important coherence and a phase shift of 180 deg). Further experimental studies are required to validate this hypothesis. Experiments relating the truncated ideal nozzles which involve only the FSS regime are under study at LEA to verify this hypothesis. The good agreement between PSD estimated by this method and that yielded by integrating the complete field of wall pressure shows the interest of this method.

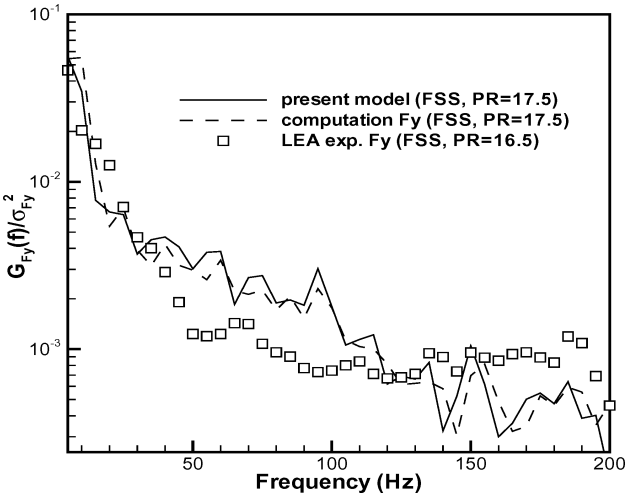

Fig. 18 PSD of the F_y component in the FSS regime.

Conclusions

This study shows the interest of calculating side loads observed in overexpanded supersonic nozzles by solving three-dimensional URANS equations.

The current simulation succeeds in simulating the hysteresis phenomenon widely observed in TOC nozzles; one can observe either the classical FSS regime or RSS regime at a prescribed constant pressure ratio, depending on the way this constant pressure ratio is established. The analyses of the flowfield suggest that, in the FSS regime, the unsteadiness probably comes from absolute instability developed in the countercurrent mixing layer formed between the ambient atmospheric air sucked into the nozzle and the main separated supersonic jet. The origin of the unsteadiness observed in the RSS regime is not clear. It seems that the perturbations coming from downstream and propagating upstream through the subsonic region found downstream of the caplike shock structure are the cause of this unsteadiness. The obtained results confirm the assumption of Nave and Coffey[4] that the side loads observed in the RSS regime are essentially due to an asymmetric reattachment of the separated flow.

The results of statistical analyses of side loads numerically recovered are in good agreement with experimental ones. For both flow separation configurations, the side loads can be seen as a rotating vector uniformly distributed within the interval $[0 : 2\pi]$ and whose magnitude follows Rayleigh's law. The PSD of side loads in the FSS regime is very different from the one of the RSS regime because the PSD of side loads in the FSS regime is dominated by very low frequencies (less than 200 Hz), whereas the PSD of side loads in the RSS regime is dominated by fluctuations at high frequencies with a peak centered around 700 Hz.

The current study also presents an efficient semi-empirical method based on wall pressure fluctuations on two opposite generating lines to assess the spectral distribution of side loads.

This study involves the free jet without external flow. In flight, the exhaust plume of nozzles merges with an external flow and this could influence the behavior of separated flow in the nozzle, especially for the case of the FSS regime. This problem will have to be further studied in the future.

Acknowledgments

This study is partly funded by Centre National d'Etudes Spatiales (CNES) within the framework of the CNES Research and

Technology Program "Aerodynamics of Nozzles and Afterbodies" under technical cooperation between the CNES/ONERA/Centre National de la Recherche Scientifique/SNECMA and EADS-LV. The authors are greatly indebted to T. Alziary de Roquefort and S. Girard from the Laboratoire d'Etudes Aérodynamiques and R. Hallard, P. Duveau, E. Garnier, and P. Guillen from ONERA for fruitful discussions.

References

[1]Summerfield, M., Foster, C., and Swan, W., "Flow Separation in Overexpanded Supersonic Exhaust Nozzles," *ARS Journal*, Vol. 24, No. 5, 1954, pp. 319–320.

[2]Lawrence, R. A., "Symmetrical and Unsymmetrical Flow Separation in Supersonic Nozzles," Ph.D. Dissertation, Inst. of Technology, Southern Methodist Univ., Dallas, TX, April 1967.

[3]Schmucker, R. H., "Status of Flow Separation Prediction in Liquid Propellant Rocket Nozzles," NASA TM X-64890, Nov. 1974.

[4]Nave, L. H., and Coffey, G. A., "Sea Level Side Loads in High-Area-Ratio Rocket Engines," AIAA Paper 73-1284, Nov. 1973.

[5]Dumnov, G. E., "Unsteady Side Loads Acting on the Nozzle with Developed Separation Zone," AIAA Paper 96-3220, July 1996.

[6]Pekkari, L. O., "Aeroelastic Analysis of Side Loads in Supersonic Nozzles with Separated Flows," AIAA Paper 94-3377, June 1994.

[7]Frey, M., and Hagemann, G., "Status of Flow Separation Prediction in Rocket Nozzles," AIAA Paper 98-2619, June 1998.

[8]Reijasse, P., Bouvier, F., and Servel, P., "Experimental and Numerical investigation of the Cap-Shock Structure in Overexpanded Thrust-Optimized Nozzles," West East High Speed Flow Field, April 2002.

[9]Takayama, K., and Ben-Dor, G., "The Inverse Mach Reflection," *AIAA Journal*, Vol. 43, No. 12 1985, pp. 1853–1859.

[10]Frey, M., and Hagemann, G., "Restricted Shock Separation in Rocket Nozzles," *Journal of Propulsion and Power*, Vol. 16, No. 3, 2000, pp. 478–484.

[11]Hagemann, G., and Frey, W., and Koschel, M., "Appearance of Restricted Shock Separation in Rocket Nozzles," *Journal of Propulsion and Power*, Vol. 18, No. 3, 2002, pp. 577–584.

[12]Tomita, T., Sakamoto, H., Takahashi, M., Sasaki, M., Tamura, H., and Tsuboi, M.,"Sub-Scale Nozzle Combustion Tests of the LE-7A Engine for Clarification of Large Side-Local (I): Formation of RSS Structure due to Combustion Condition," AIAA Paper 2002-3842, July 2002.

[13]Watanabe, Y., Sakazume, N., and Tsuboi, M., "LE-7A Engine Nozzle Problems During the Transient Operations," AIAA Paper 02-3841, July 2002.

[14]Ostlund, J., Damgaard, T., and Frey, M., "Side-Load Phenomena in Highly Overexpanded Rocket Nozzles," AIAA Paper 2001-3684, July 2001.

[15]Terhardt, M., and Hagemann, G., "Flow Separation and Side-Load Behaviour of the Vulcain Engine," AIAA Paper 99-2762, June 1999.

[16]Girard, S., Deniau, H., Nguyen, A. T., and Alziary de Roquefort, T., "Etude de Pécoulement dans une Tuyère Propulsive à Contour Parabolique en Régime Surdétendu," *37eme Colloque d' Aérodynamique Appliquée, Aérodynamique et Propulsion des Véhicules à Grande Viless*, AAAF, March 2001.

[17]Reijasse, Ph., Morzenski, M., Naudin, P., and Geneau, F., "Fluctuating Side-Load Measurements in Overexpanded Subscale Rocket-Nozzles," AIAA Paper 2001-3557, July 2001.

[18]Munier, D., Garcon, F., Champigny, P., Deck, S., and Hallard, R., "Side Load Measurements on Subscale Launcher Nozzles," *4th International Conference on Launcher Technology 'Space Launcher Liquid Propulsion*,' Dec. 2002.

[19]Chen, C. L., Chakravarthy, S. R., and Hung, C. M., "Numerical Investigation of Separated Nozzle Flows," *AIAA Journal* Vol. 32, No. 9, 1991, pp. 1836–1843.

[20]Groß, A., and Weiland, C., "Investigation of Shock Patterns and Separation Behavior of Several Subscale Nozzles," AIAA Paper 2000-3293, July 2000.

[21]Ostlund, J., and Jaran, M., "Assessment of Turbulence Models in Overexpanded Rocket Nozzle Flow Simulations," AIAA Paper 99-2583, June 1999.

[22]Onofri, M., Nasuti, F., and Bongiorno, M., "Shock Generated Vortices and Pressure Fluctuations in Propulsive Nozzles," AIAA Paper 98-0777, Jan. 1998.

[23]Nasuti, F., and Onofri, M., "Viscous and Inviscid Vortex Generation During Startup of Rocket Nozzles," *AIAA Journal*, Vol. 36, No. 5, 1998, pp. 809–815.

[24]Takahashi, M., Ueda, S., Tomita, T., Takahashi, M., Tamura, H., and Aoki, K., "Transient Flow Simulation of a Compressed Truncated Perfect Nozzle," AIAA Paper 01-34363, July 2001.

[25]Takahashi, M., Tomita, T., Sakamoto, H., Tamura, H., Watanabe, Y., and Tsuboi, M., "Influence of a Gap for Film Cooling on Transient Flow Characteristics of Rocket Engine Nozzles," AIAA Paper 02-4147, July 2002.

[26]Yonezawa, K., Yokota, K., Watanabe, Y., Tsujimoto, Y., and Abe, T., "2-D Numerical Simulation of Side Loads in Rocket Nozzles," *23rd International Symposium on Space Technology and Science*, May 2002.

[27]Morinigo, J. A., and Salva, J. J., "Numerical Investigation of the Separation Modes Transition and Hysteresis in the Sub-Scale J2S Rocket Engine Nozzle," *4th International Conference on Launcher Technology 'Space Launcher Liquid Propulsion*,' Dec. 2002.

[28]Deck, S., and Guillen, Ph., "Numerical Simulation of Side Loads in an Ideal Truncated Nozzles,"*Journal of Propulsion and Power*, Vol. 18, No. 2, 2002, pp. 261–269.

[29]Deck, S., Hallard, R., and Guillen, Ph., "Numerical Simulations of Steady and Unsteady Separated Nozzle Flows," AIAA Paper 02-0406, Jan. 2002.

[30]Deck, S., Garnier, E., and Guillen, P., "Turbulence Modelling Applied to Space Launcher Configurations," *Journal of Turbulence*, Vol. 3, No. 57, 2002, pp. 1–21.

[31]Deck, S., and Hallard, R., "Numerical Simulations of Launcher Nozzle Flows and Side Loads," *4th International Conference on Launcher Technology 'Space Launcher Liquid Propulsion*,' Dec. 2002.

[32]Yonezawa, K., Yokota, K., Tsujimoto, Y., Sakazume, N., and Watanabe, Y., "Three-Dimensional Unsteady Flow Simulation of Compressed Truncated Perfect Nozzles," AIAA Paper 02-3991, July 2002.

[33]Péchier, M., "Prévisions Numériques de l'Effet Magnus pour des Configurations de Munition," Ph.D. Dissertation, Dept. of Mechanical Engineering, Université de Poitiers, Poitiers, France, Sept. 1999.

[34]Péchier, M., Guillen, Ph., and Caysac, R., "Magnus Effect over Finned Projectiles," *Journal of Spacecraft and Rockets*, Vol. 38, No. 4, 2001, pp. 542–549.

[35]Girard, S., "Etude des Charges Latérales dans une Tuyère Supersonique Surdétendue," Ph.D. Dissertation, Dept. of Mechanical Engineering, Université de Poitiers, Poitiers, France, Sept. 1999.

[36]Goldberg, U. C., "Separated Flow Treatment with a New Turbulence Model," *AIAA Journal*, Vol. 24, No. 10, 1986, pp. 1711–1713.

[37]Ramakrishnan, S., and Goldberg, U. C., "Numerical Simulation of Swept Shock/Boundary-Layer Interactions," AIAA Paper 90-5234, Oct. 1990.

[38]Alziary de Roquefort, T., "Low Frequency Fluctuations in Separated Turbulent Compressible Flows," *Symposium on Advanced Fluid Information*, Dec. 2002.

[39]Nguyen, A. T., Deniau, H., Girard, S., and Alziary de Roquefort, T., "Wall Pressure Fluctuations in an Over-Expanded Supersonic Nozzle," AIAA Paper 2002-4001, July 2002.

[40]Strykowski, P. J., Krothapalli, A., and Jendoubi, S., "The Effect of Counterflow on the Development of Compressible Shear Layers," *Journal of Fluid Mechanics*, Vol. 308, July 1996, pp. 63–96.

[41]Terhardt, M., Hagemann, G., and Frey, M., "Flow Separation and Side-Loads Behavior of Truncated Ideal Rocket Nozzles," AIAA Paper 2001-3686, July 2001.

[42]Bendat, J. S., and Piersol, A. G., *Random Data: Analysis and Measurements Procedures*, Wiley-Interscience, New York, 1971.

[43]Welch, P. D., "The Use of Fast Fourier Transform for the Estimation of Power Spectra: A Method Based on Time Averaging over Short Modified Periodograms," *IEEE Transactions on Audio and Electroacoustics*, Vol. AU-15, No. 2, 1967, pp. 70–73.

[44]Kay, S., *Modern Spectral Estimation. Theory and Application*. Prentice–Hall, Upper Saddle River, NJ, 1987, pp. 72–77.

[45]Nguyen, A. T., Deniau, H., Girard, S., and Alziary de Roquefort, T., "Unsteadiness of Flow Separation and End-Effects Regime in a Thrust-Optimized Contour Rocket Nozzle," *International Journal of Flow, Turbulence, and Combustion*, Vol. 71, No. 1, 2003, pp. 161–181.

H. Reed
Associate Editor